Tracking dry intrusions on satellite water vapour imagery and model output for data assimilation of potential vorticity pseudo-observations

By Y. MICHEL and F. BOUTTIER

National Center for Meteorological Research (METEO-FRANCE, CNRM)
Numerical Weather Prediction Department (GMAP)
42 av. Gaspard Coriolis, 31057 Toulouse Cedex, France

A satellite image processing technique has been developed for the identification and tracking of upper tropospheric features related to mid-latitude synoptic scale cyclogenesis. Persistent warm radiance features are detected on water vapour (WV) images using an adaptive thresholding technique and tracked using estimations of the motion of the features based on cross-correlation of successive images. These features are then screened using both image-based (time persistence and warming rate) and model-based criteria (relative position to a jet streak). The aim is the characterization of dry intrusions of stratospheric air into the upper troposphere. On a selected sample of events, the resulting trajectories prove to be very consistent with the subjective identification of cyclogenesis events on imagery. In accordance with potential vorticity (PV) theory, the detected warm features are correlated with positive anomalies of potential vorticity. This identification technique can be applied to model output thanks to the use of a radiative transfer model, which suggests future applications in forecast verification. An automatic geometrical association algorithm links model and satellite cells to provide guidelines for the specification of pseudo-observations of PV in the ARPEGE 4D-Var assimilation scheme. Observations are build to correct the displacement and the amplitude error, the last one being derived from the radiance temperature of the cells. Problems arising when comparing PV and WV radiances along trajectories are described. 4D-vary assimilation of PV pseudo-observations is finally illustrated on a case study of a cyclogenesis.

Detection and tracking of dynamical warm features on satellite water vapour images

Application of an adaptive thresholding algorithm

Infrared radiations measured by meteorological satellites into the water vapour (WV) bands (around $6.3\mu m$) provide useful information to forecasters on the flow patterns associated with mid and upper levels (Weldon and Holmes, 1991). In particular, upper level PV anomalies involved in cyclogenesis (Hoskins $et\ al.$, 1985) are often visible as localized warm features on WV imagery that can be visually tracked for hours.

T_{min}	Minimum temperature of threshold	-38^oC
T_{max}	Maximum temperature of threshold	-8^oC
ΔT_d	Minimum depth of temperature for a cell	2.2^oC
S_{min}	Minimum area for a cell	2000 km^2
ΔT_i	Thresholding increment	0.3^oC

Table 1: The parameters of the adaptive thresholding algorithm

The algorithm used here has been derived from the ISIS thunderstorm detection system that locates cold cloud tops on sequences of infrared satellite images (Morel and Sénési, 2002). Here it is applied in reverse (i.e. warm features are detected instead of cold ones) and with some modifications, the most important one being the use of an adaptive thresholding strategy inspired by Peak and Tag (1994). The main parameters of this algorithm are the thresholding intervals [T_{min}, T_{max}], the minimum depth of temperature and surface for cells ΔT_d and S_{min} (see Table 1). The algorithm is described in Michel and Bouttier (2006) and Morel and Sénési (2002).

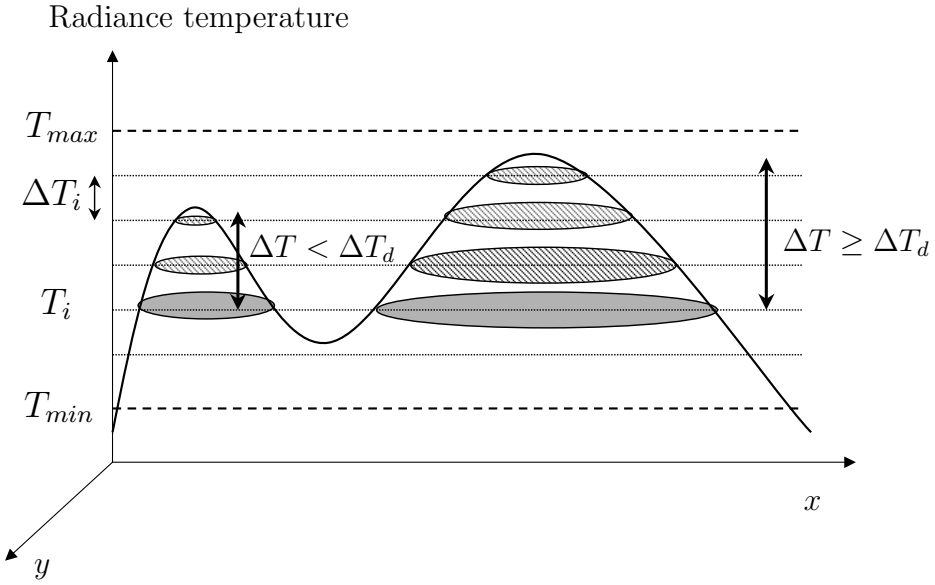

Figure 1: Schematic view of the adaptive thresholding technique for radiance temperatures T_i between T_{max} and T_{min} at resolution ΔT_i.

The parameters of the detection method have been set to maximize warm features detections that are associated with the cyclones on a learning test sample (Table 1). The learning test sample is made of twenty cyclonic events over the North Atlantic and Europe, including several historically violent storms (from the Météo-France database) as well as other unexceptional events covering different synoptic situations (from Santurette and Georgiev, 2005).

Screening of upper-level dynamical features

Image-based criteria

The precedent thresholding algorithm detects cells that are not always linked with upper-level dynamics, so that additional selection procedure is needed. Some standard image-based selection rules are applied by forecasters: time-persistence, warming rates and upstream convective development (Santurette and Georgiev, 2005). We use the learning test sample to specify additional filtering criteria that will select dynamically important cells (Michel and Bouttier, 2006).

Lifetime of trajectories. The requirement of a minimum lifetime of three hours yields an efficient reduction of spurious detections, while still allowing most cyclogenetic events to be retained just a few hours after they become visible on the images.

Temperature evolution in trajectories. During the lifetime of a cyclone, the corresponding features usually start by warming up quickly, then the radiance temperature stabilizes, then the features cool down. Temperatures T_t are computed as maximum radiance temperatures over the surfaces of the cells. Therefore, a filter based on this evolution has been implemented: we require that a given trajectory is only selected if its temperature variation since its first detection $T_t - T_0$ meets the empirical criterion:

$$T_t - T_0 > \tau \left(1 - \frac{1}{\pi} \arctan \left(\frac{T_t - T_{ref}}{\Delta T_{ref}} \right) \right) \tag{1}$$

$$\text{with } \tau = 1.5^o C/3H, T_{ref} = -34^o C \text{ and } \Delta T_{ref} = 1^o C \tag{2}$$

The criterion is more stringent for colder features in order to limit the number of false alarms and based on the learning sample (Michel and Bouttier, 2006).

Model-based criteria

According to the conceptual model of mid-latitude PV dynamics and to forecaster experience, cyclogenesis is expected to occur in the vicinity of a strong upper level jet on the cyclonic side. We resort to using NWP numerical model products, which are available in real time with global coverage. This information is likely to contain forecast errors, so that we will only consider large scale wind, which tends to be more predictable than small scale features.

Distance to the jet. The computation of a distance to the jet requires the definition of a line of maximum wind speed to characterize the jet core. This is done using an image processing technique, called skeleton transformation, on the set of pixels where the wind speed is greater than a predefined threshold (30 ms^{-1} at 300 hPa). The distance d_{jet} between a warm feature and the nearest jet core is found by searching for the closest pixel that belongs to a core (figure 2).

Location on the cyclonic side of the jet. The last selection criterion considered in this study is the position with respect to the nearest jet core. The characteristics of the cells of the learning dataset are extracted and plotted on the histogram presented in figure 3.

We filter trajectories with the following joint criterion based on the jet distance d_{jet} and the angle

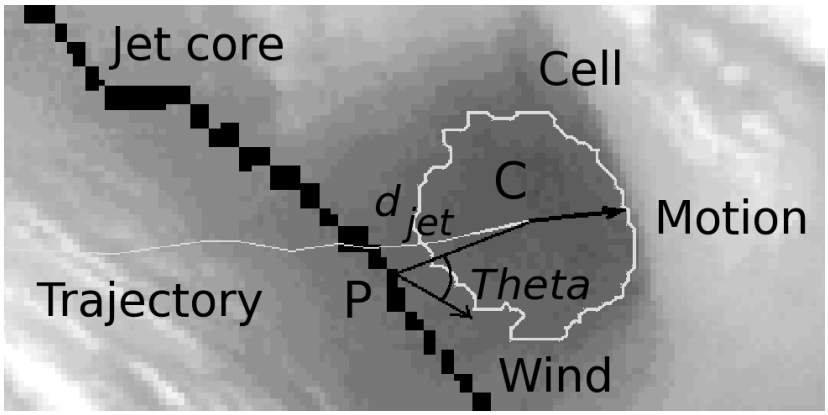

Figure 2: Sketch of the relative position of a cell with respect to the jet, extracted from results on 16 December 2004, 12 UTC. C is the gravity center of the cell and P the closest point on the jet core. The distance to the jet is $d_{jet} \equiv \| CP \|$, the angle θ is between CP and the wind at point P. The cell is contoured in white. Also shown the wind vector at point P and the estimated motion of the cell at point C.

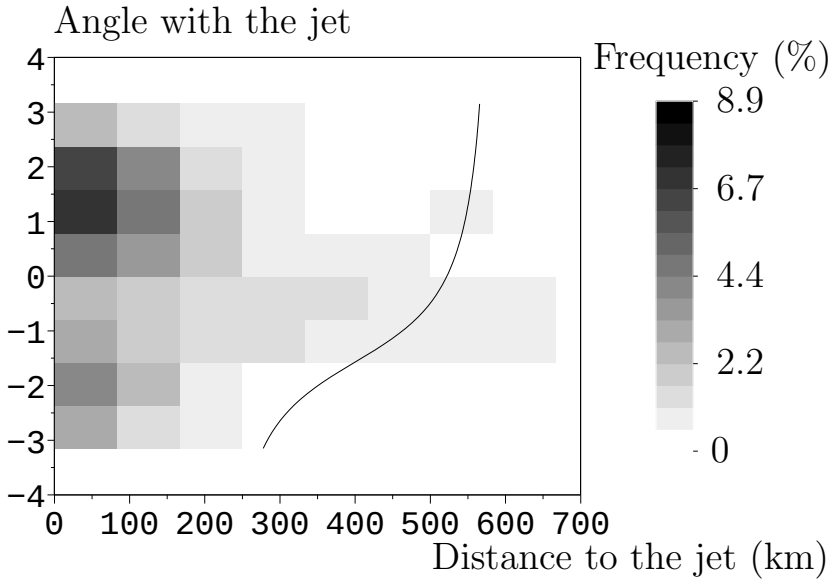

Figure 3: Distribution of the cells from the test sample (Table 1) in the plane formed by the distance (length of category: 80 km) and the angle with the jet (length of category: $\frac{2\pi}{8}\ rad$). The curve shows the decision boundary for the jet proximity criterion associated with $d_{jet} = 400\ km$.

with the jet θ:

$$d_{jet} > d_c \left(1 + \frac{1}{\pi} \arctan\left(\frac{\theta - \theta_{ref}}{\Delta\theta_{ref}}\right)\right) \quad (3)$$

$$\text{with } d_c \simeq 400\ km,\ \theta_{ref} = -\frac{\pi}{2} \text{ and } \Delta\theta_{ref} = \frac{\pi}{3} \quad (4)$$

This empirical function matches the distribution of the characteristics of the features (figure 3) from the learning dataset and is more stringent for the cells that are on the anti-cyclonic side of the jet. Warming rate and position with respect to the jet are likely to be used for the selection of warm areas that are linked with upper-level dynamics.

Validation of the algorithm

To further validate the performances of the algorithm, we have applied it to an independent test sample of situations that are taken over year 2004 from the Météo France dangerous events database. To evaluate the real-time performance of the algorithm, we look at the cells detected by the thresholding algorithm (before any selection procedure) and generate a sample made of cells that are linked with upper-levels dynamics. The ground truth for building the verifying samples is a forecaster's decision. We compute false alarms rates (FAR) and probabilities of good detections (POD) as

$$FAR = \frac{N_{false}}{N_{hits} + N_{false}} \text{ and } POD = \frac{N_{hits}}{N_{sample}}$$

where:

- N_{hits} is the number of relevant cells that are detected after filtering (hits).
- N_{false} is the number of spurious cells that are detected after filtering (false alarms).
- N_{sample} is the size of the sample of relevant cells.

We use a cell count rather than a trajectory count to evaluate the detection in a six-hour assimilation cycle. The FAR reaches values of 0.7-0.85 whereas the POD reaches 0.15-0.25 depending on the decision parameters (Michel and Bouttier, 2006). Some improvement could however be expected from other sources of information (such as satellite-based estimations of cloud cover) by removing the spurious cells that are still present in cloudy areas.

Using pseudo-observations in data assimilation

4D-Var, direct assimilation of radiances and pseudo-observations

The current emphasis in the data assimilation community is on the direct use of satellite radiances rather than retrievals of atmospheric temperature and humidity profiles as the last ones do not take into account cross-correlation errors with the background (Joiner and Dee, 2000) and are therefore suboptimal. 4D-Var assimilation of WV geostationary Clear Sky radiances (CSR) has proven to be beneficial for the analysis of the humidity and of the upper-level wind fields especially in the tropical

region (Köpken *et al.*, 2004). 4D-Var through the coupling of wind and humidity in the tangent-linear model (TLM) is indeed able to partly infer the wind from radiance observations. This has been studied in the ideal context of a 1D Extended Kalman Filter and constituent assimilation by Daley (1995) and highlighted in a realistic context of water vapour ATOVS radiances assimilation by Andersson *et al.*(1994).

However pseudo-observations, for example of tropospheric winds derived from humidity features tracking in WV channels (Velden *et al.*, 1997), have not disappeared despite their contamination with large-scale spatial errors (Bormann *et al.*, 2003). Synthetic "bogus" surface pressure observations are successfully used in analyses of the Southern Hemisphere and the tropical atmospheres, e.g. for positioning tropical cyclones (Pu and Braun, 2001). This work investigates whether one can generate reliable pseudo-observations of dry intrusions associated with mid-latitude cyclones from sequences of geostationary satellite images in order to correct alignment and amplitude errors in backgrounds fields (see Lawson and Hansen 2005 for a discussion on additive and alignment errors).

Preliminary testing of direct WV radiances assimilation shows that the dynamical impact is weak for the mid-latitudes. Guérin *et al.*(2006) argue that upper-level temperature and humidity increments have a weak impact on dynamical fields. The covariances implied by the current multivariate formulation of B are not fully described in observation space (only the variances are being studied by Andersson *et al.*, 2000), so that this issue requires further study. Snyder *et al.*(2003) show in a quasigeostrophic model that error covariances rapidly (within one day) exhibit a strong spatial correlation between the PV variance and the magnitude of the reference-flow PV gradient and that these characteristics can survive the assimilation of observations. We therefore suggest that the B specification may not be accurate enough to fairly represent the temperature and humidity correlation with vorticity is these localized regions, and that its implicit evolution in 4D-Var over an assimilation window of six hours may not either (see also Fischer *et al.*, 1998). However this assumption has still to be proven and will be the topic of a future study. B and its temporal evolution can be inferred from random estimations (Andersson *et al.*, 2000):

$$B \simeq \frac{1}{N_{BGVECS}} \sum_{i=1}^{N_{BGVECS}} (B^{1/2}\xi_i)(B^{1/2}\xi_i)^T \text{ where } \xi_i \sim \mathcal{N}(0,1)$$

So that the projection of B in observation spaces H_1 and H_2 can be diagnosed through:

$$H_1 B H_2^T \simeq \frac{1}{N_{BGVECS}} \sum_{i=1}^{N_{BGVECS}} (H_1 B^{1/2}\xi_i)(H_2 B^{1/2}\xi_i)^T \text{ where } \xi_i \sim \mathcal{N}(0,1)$$

It is therefore possible, using for H_1 observations of dynamical quantities such as wind or PV and for H_2 observations of radiances to study the projection of analysis increments in observation space H_1:

$$H_1 \underline{\delta_x} = H_1 B H_2^T (H_2 B H_2^T + R_2)^{-1} \underline{d}_2$$

(where B and R denote respectively background and observation error covariances, $\underline{d}$ is the innovation vector $\underline{y_o} - H(\underline{x_b})$) and in a 4D-Var analysis where B is implicitly evolved in time with the linear

perturbation model L:

$$H_1\underline{\delta_x} = H_1 L B L^T H_2^T (H_2 L B L^T H_2^T + R_2)^{-1} \underline{d}_2$$

This can be used to study to what extent the assimilation of WV radiances has an impact on PV initial state, or also to study the background error in PV space (*e.g.* $H_1 = H_2 = H_{PV}$). Examples of background variances projected in PV space for a static B (*e.g.* in a 3D-Var framework) will be presented in the next section. One possibility would be to locally specify correlations in B to recover PV-balanced increments in the region where the radiances seem to be linked with the upper-level dynamics. This is not feasible in a real variational data assimilation system where B is specified in the spectral space, but a wavelet approach for B might be more successful.

Furthermore, linear data assimilation system would be able to produce realistic increments only in the case where the displacement error is small compared to the vortex size (for linearity reasons, as reported by Lawson and Hansen,2005). Therefore the approach of building pseudo-observations and assimilating them in a 4D-Var is studied further in this paper. Weaknesses of this approach will be also highlighted.

Modifications of the PV initial state

Actually, in case of a strong failure of the system to provide a good background state, PV modifications are often introduced manually. This is very similar to tropical cyclone bogussing. Røsting $et\ al.$(2003, 2006) introduce PV modifications to the initial state using PV inversion and singular vectors to solve the height assignment problem. The vertical PV structure of the leading singular vectors and the WV images are used to diagnose the full 3D structure of the modifications. It is clear however that these details should be as much as possible produced by the data assimilation algorithm itself, to take into account several temporal position and amplitude observations as well as the statistics associated with observation errors. Other well-known advantages include more consistency with the model dynamics, resolution and physics (Pu and Braun, 2001).

The observation operator and the error variances

The goal is to incorporate pseudo-observations of dynamical quantities such as PV, surface pressure or relative vorticity ξ. There may be a need for a special observation operator H inside the variational assimilation scheme.
A PV operator, its tangent-linear and its adjoint versions based on a simplified form of Ertel PV have been implemented into the ARPEGE assimilation scheme (Guérin $et\ al.$, 2006).

$$H_{PV} = -g\xi_a \frac{\partial \theta}{\partial p} - g\frac{fp}{R}\left(\frac{p_0}{p}\right)^{R/C_p}\left[\left(\frac{\partial U}{\partial p}\right)^2 + \left(\frac{\partial V}{\partial p}\right)^2\right]$$

The conditioning of the 4D-Var minimization is weakly affected by the PV operator leading to good convergence, as no cross terms between the balanced and the unbalanced part of model variables appear in the Hessian due to the particular PV observation operator (Appendix B of Guérin $et\ al.$,

2006).

The assimilation of pseudo-observations of relative vorticity is straightforward, as ξ is part of the control variable of the minimization problem (Derber and Boutier, 1999).

The observation error variance depends on the way these pseudo-observations are produced and will be discussed in the next section for PV observations.

The background error variances are diagnosed through randomization:

$$H_{PV} B H_{PV}^T \simeq \frac{1}{N_{BGVECS}} \sum_{i=1}^{N_{BGVECS}} (H_{PV} B^{1/2} \xi_i)(H_{PV} B^{1/2} \xi_i)^T \text{ where } \xi_i \sim \mathcal{N}(0,1)$$

Variance maps for σ_b^{PV} highlight regions where the data assimilation scheme would give large weight to PV observations. An example is shown on figure 4 with the meteorological background shown in figure 5. Strong values of σ_b^{PV} are connected with meteorological features such as pronounced tropopause gradients (Snyder *et al.*, 2005) and as the low over Island.

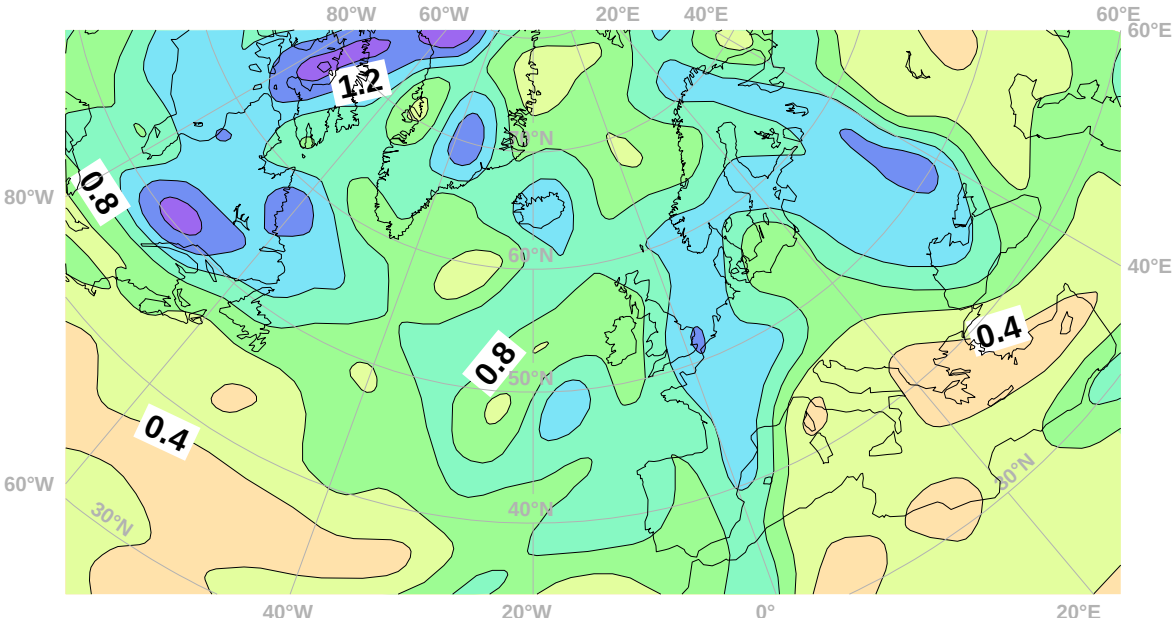

Figure 4: σ_b map in PV space valid for 01 December 2006, 06 UTC as deduced from a randomization with $N_{BGVECS} = 100$ (the accuracy is of the order of $1/2\sqrt{N_{BGVECS}}$). Contouring every 0.2 PVU. Truncation T107 at model level 25 (about 435 hPa).

Building pseudo-observations using displacement and amplitude errors

Satellite images are daily used to monitor NWP output in terms of displacement and intensity errors. We consider doing this automatically by processing model output imagery. The procedure described above has been applied to synthetic satellite images produced by the operational global model of Météo-France, ARPEGE, post-processed on the same domain as satellite images at a resolution of 0.2 degree. Radiances are produced by the RTTOV radiative transfer simulation software for the relevant imager. The detection and screening procedures behave much as if satellite images were used.

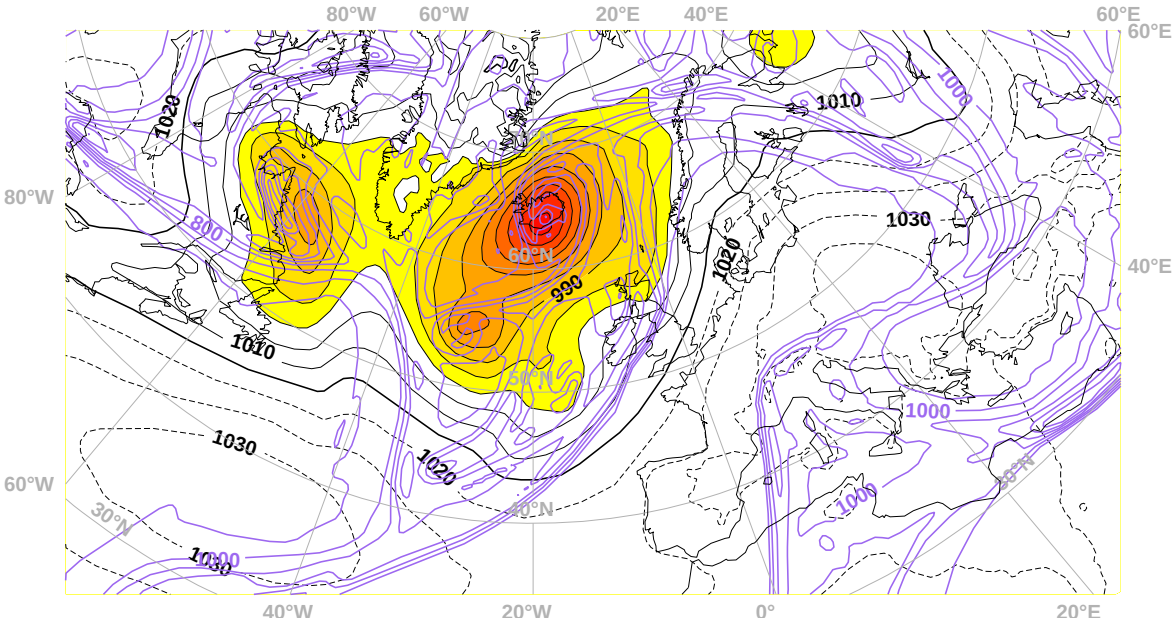

Figure 5: Meteorological background valid for 01 December 2006, 06 UTC (an ARPEGE 6 hours forecast). Geopotential of the 1.5 PVU surface (lavender contours every 100 dam, only where $Z \leq 1100$ dam) and Mean-Sea Level Surface Pressure (black contours every 5 hPa, shaded when $P_{mer} \leq 1000$ hPa). Truncation T358.

A geometrical association procedure has been developed to compare the satellite and the model dry intrusions: each feature detected on the model output is *associated* with the closest satellite imagery feature if it is nearer than $d_{assoc} = 1000\ km$. When one considers our learning sample of cyclonic events, 85% of the simulated ones are associated, versus 70% of the observed ones. In other words, a majority of dry intrusions is automatically detected and associated in both model and satellite imagery. This procedure allows to study distortion and amplitude errors as introduced by Hoffman *et al.*, 1995 (see also the figure 6).

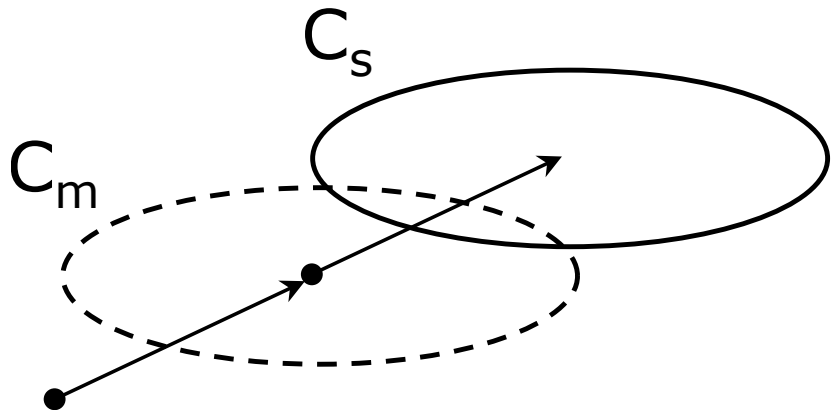

Figure 6: The distortion and amplitude errors in the comparison of a satellite (C_s) and a model cell (C_m).

Provided that the satellite (C_s) and the model (C_m) cells are linked for a sufficient time (here 6 hours), pseudo-observations are build in either a monopole or dipole configuration (figure 6). Denoting by $\mathcal{G}$ the gravity center of the cells and by f a dynamical field (f_b for the background, f_0 for the pseudo-observed field), one can build pseudo-observations at the satellite position $\mathcal{G}(C_s)$ and at the model position $\mathcal{G}(C_m)$ for f observations by:

$$f_o\big[G(C_s)\big] = f_b\big[G(C_m)\big] + \Delta_f(C_s, C_m)$$
$$f_o\big[G(C_m)\big] = f_b\big[G(C_m) - \overrightarrow{G(C_m)G(C_s)}\big])$$

$\Delta_f(C_s, C_m)$ is the amplitude correction and depends on both cells characteristics and of the dynamical link between radiances and the field f. In this case, f would be potential vorticity for the extra-tropical cyclone problem, or surface pressure or relative vorticity for the tropical cyclone problem (Pu and Braun, 2000). The dynamical link between WV radiances and PV is explored further in the next section. In the case where no cells are present in either the imagery or the model, a first approximation consists of trying to apply the same algorithm with a zero displacement error. We see that there is **a height problem assignment** for f (this is of course general for pseudo-observations based on bidimensionnal imageries rather than on outputs from atmospheric sounders). Choosing f is in a way quite similar to building a balance in B for traditional observations. The second observation at the model cell position $f_o\big[G(C_m)\big]$ only corrects the displacement error and assumes that it is spatially uniform. One could imagine other forms for the displacement error possibly including an observation displacement error and a model of its spatial distribution (as first proposed by Lawson and Hansen, 2005).

4D-Var assimilation of PV and amplitude correction: the PV - WV relationship

The practical problem is to translate the detected feature information into observations that can be assimilated. It is suggested that model/observation radiance inconsistencies tend to be related to PV errors in dynamically active areas. PV is an attractive parameter to assimilate in 4D-Var, because it is more directly related to linearized model dynamics than radiances. Modifying the upper-level PV fields of the initial state has proven to be an efficient way to correct forecasts of cyclogenesis, as shown by Demirtas and Thorpe (1999) using PV inversion procedures. However it remains challenging even for a trained forecaster, as pointed out by Swarbrick (2001).

Various authors have attempted to establish a quantitative relationship between PV and WV radiance temperatures using different approaches. For example, Georgiev (1999) reports significant correlation with linear regression between WV data and PV at 500 hPa (where samples are however restricted to localized areas and limited by a threshold condition PV>1.2 PVU). Pankiewicz *et al.*(1999) investigate a regression using an artificial neural network between WV radiances and PV on the 315 K isentropic surface. Complicating factors in the PV-WV relationship are listed by several authors (Demirtas and Thorpe, 1999; Georgiev, 1999 and Swarbrick, 2001) and include WV dependence with vertical profiles of temperature and degradation caused by inconsistencies between model and observations.

Relationship between temperatures of the cells and PV fields in model trajectories

We therefore work with synthetic WV images from RTTOV so that there is no model error degrading the PV-WV relationship. Michel and Bouttier (2006) exhibit six situations where a clear qualitative agreement along time could be seen between the temperatures of the cells (6.3 μm MVIRI channel simulated with RTTOV) and the averaged PV values of the cells on a isobaric level (at 400 hPa where the water vapour channels peaks). We post-process fields of PV on isobaric levels from 800 to 50 hPa and extract vertical profiles of PV averaged under the surfaces of the detected cells. The 1.5 PVU height H_{Tropo} is computed as a log-interpolation of the lowest height where $PV(H_{Tropo}) = 1.5$ PVU. We compare the temperatures of the cells with the value of PV at 400 hPa ($PV_{400\ hPa}$), with H_{tropo} and with vertical averages of PV $\int_{\mathcal{H}} PV(h)e^{-\left(\frac{h-H_{Ref}}{\Delta H}\right)^2} dh$ ($H_{ref} = 400\ hPa, 550\ hPa$ and $\Delta_H = 200\ hPa$).

The figure 7 shows the evolution of these parameters along time (following the tracking) for a trajectory of a dry intrusion detected by the algorithm on 18/11/2004. The agreement is very good between the temperature and the PV evolution of the cell with a correlation ranging 0.85 (the linear regression shown on the right panel of figure 7).

The figure 8 shows the evolution of temperature and H_{Tropo} along time (following the tracking) for a trajectory of a dry intrusion detected by the algorithm on 20/05/2006. The agreement is greatly improved when temperature jumps at assimilation times are canceled. H_{Tropo} exhibits a spurious jump at $t_0 + 18$ hours related to its definition which is not continuous with the PV vertical profile.

The PV amplitude correction

As shown in the previous example, some factors degrade the PV-WV relationship. We have extracted the PV profiles associated with 10 trajectories of cells tracked in the model imagery. No parameter between H_{Tropo}, $PV_{400\ hPa}$ or vertical averages of PV performs better than the others on all cases. The PV-WV relationship needs to take into account:

- potential horizontal shifts between the PV and the WV fields (e.g. because of a tropopause foliation);
- the vertical level attribution (especially when PV anomalies do not reach the standard 1.5 PVU value).
- temperature jumps at analysis time when using 4D-Var trajectories due to temperature at humidity increments (c.f. figure 7);

Local maxima can be detected along the vertical profile of PV, thus providing a basis for studying the second point. The horizontal shifts that sometimes occur between PV and the WV fields seem more difficult to handle automatically, and further work is needed on this issue.

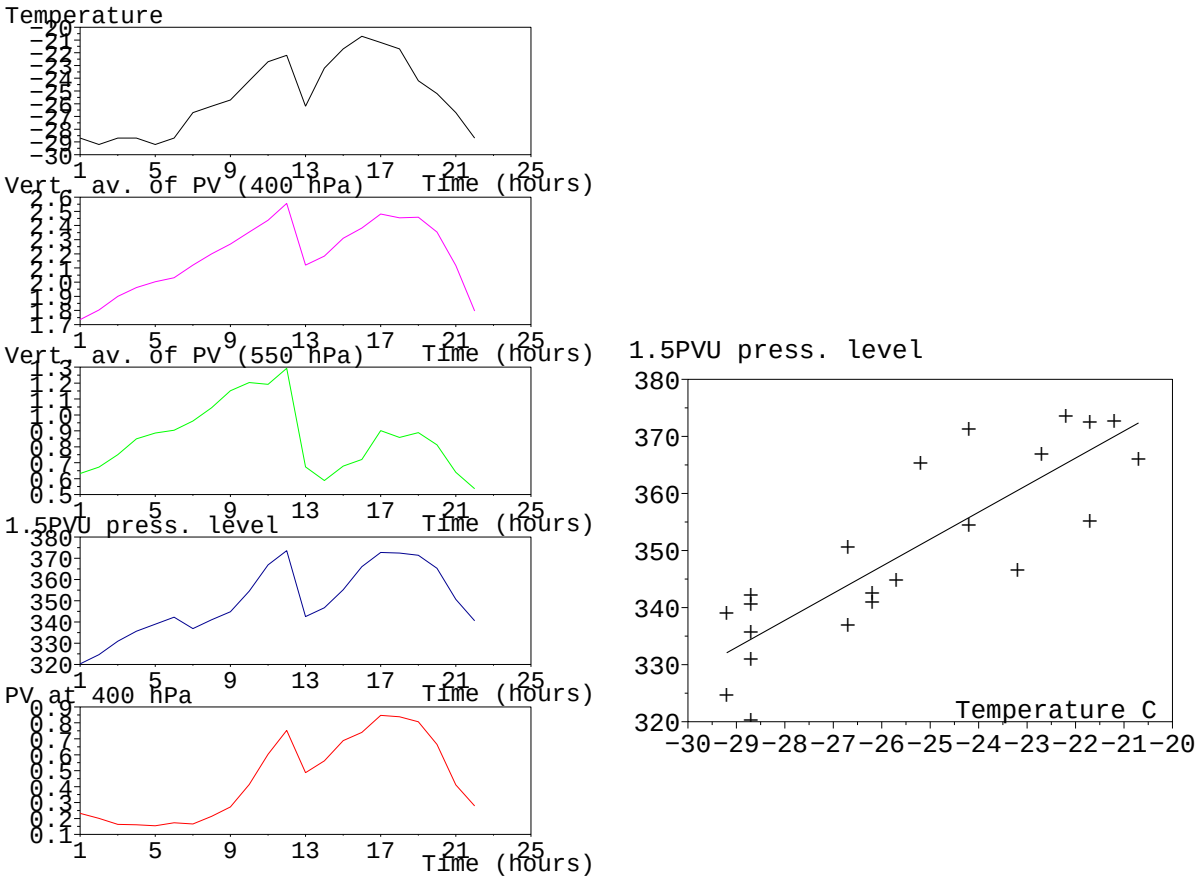

Figure 7: Evolution of the maximum temperatures (lower curves),of $PV_{400\ hPa}$, H_{tropo} and vertical averages of PV for the trajectory in the model imagery (ARPEGE 4D-Var trajectories associated with radiative transfer RTTOV for SEVIRI $6.2\mu m$ channel). Time is in hours since first detection and starts 18/11/2004 06UTC. Right panel: linear regression between temperature and H_{Tropo}, correlation coefficient=0.85

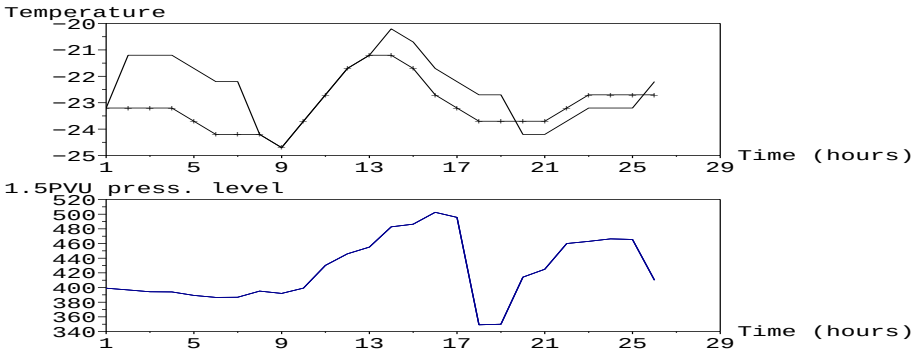

Figure 8: Evolution of the maximum temperatures (upper panel, with crosses when corrected from temperatures gaps at assimilation times) and of H_{tropo} (lower panel) for the trajectory in the model imagery (ARPEGE 4D-Var trajectories associated with radiative transfer RTTOV for SEVIRI $6.2\mu m$ channel). Time is in hours since first detection and starts 20/05/2006 05UTC.

A case study of cyclogenesis

A brief synoptic description

On 26^{th} May 2006, ARPEGE model overestimated the development of a cyclonic event over the Atlantic (figure 9). This spurious development occurred in a breaking jet flow. A potential vorticity anomaly placed in a confluence entrance of the jet exhibits rapid growth to lead to a cyclogenesis 24 hours later. Almost all forecast ranges prove to be erroneous as compared to the observations (not shown) or the analysis (figure 9) by overestimating the development.

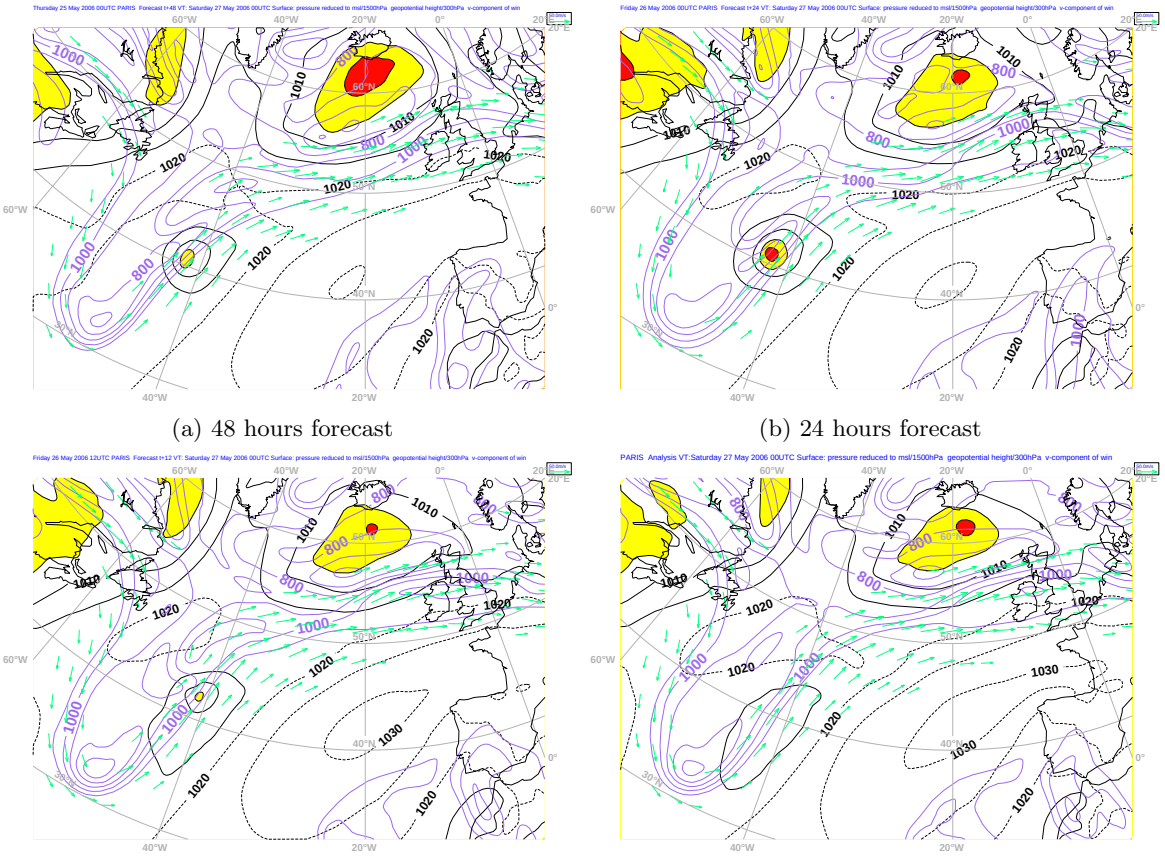

(a) 48 hours forecast

(b) 24 hours forecast

(c) 12 hours forecast

(d) Analysis

Figure 9: Analysis and ARPEGE forecast valid for 27 May 2006, 00UTC. Wind at 300 hPa (only force superior to 30 m s^{-1}, green arrows), surface pressure (dashed above 1020 hPa, solid bold at 1015 hPa, solid under 1010 hPa, every 5 hPa), 1.5 PVU height (every 100 dam starting 1100 dam, violet contours).

Application of the tracking algorithm

We applied the above detection and tracking algorithm to both MSG and model output water vapour images (figure 10). The algorithm selects two cells on the model imagery in the vicinity of the region of interest (35N, 50W) as shown on figure 10. They are also clearly visible on upper level dynamics

as shown by the model potential vorticity fields (figure 11). One of these cells is also present in the MSG satellite imagery but with a visible displacement error.

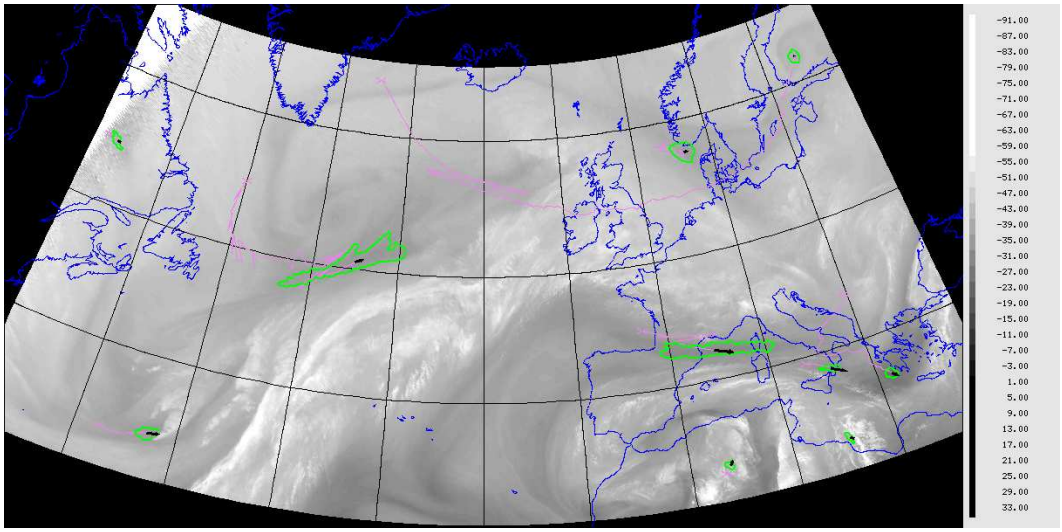

(a) MSG

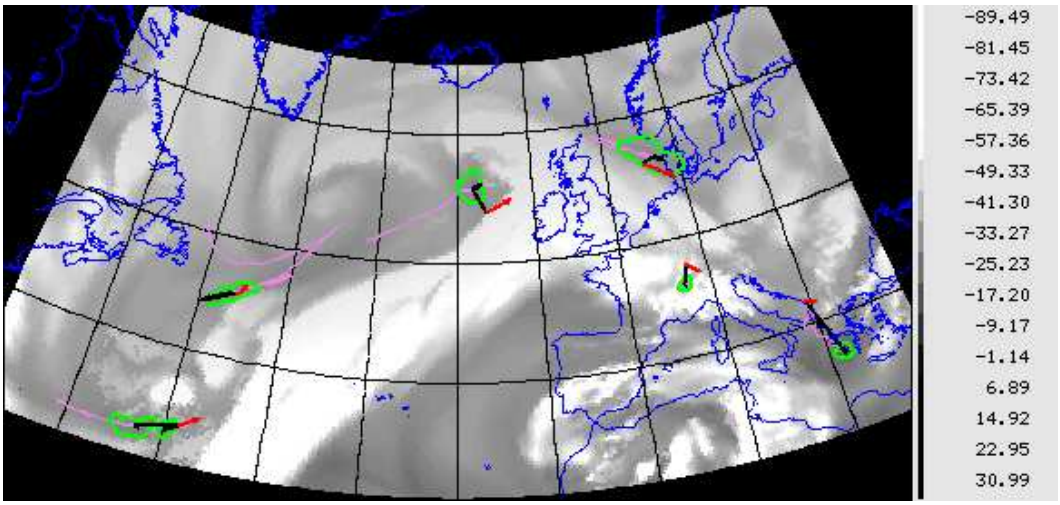

(b) ARPEGE+RTTOV

Figure 10: Comparison of results of the algorithm on water vapour images on 26 May 2006 03 UTC, as provided by MSG 6.2μm images (upper panel) and RTTOV with ARPEGE forecast (lower panel). Bold green contours delineate cells and thin purple line show trajectories (starting with a cross). Radiance temperatures are in Celsius. The cyclogenesis of interest is on the lower left corner near 30N, 55W.

Introduction of PV observations

PV observations are introduced using the preceding described method but using only the displacement error. They are introduced every hour of the 6 hours data assimilation window with a specified observation error $\sigma_o = 0.2\ PVU$. The 4D-Var allows a flow dependent and time-consistent correction of the PV initial state (see the PV increment on figure 13). The new analysis PV field (figure 11) has

a displaced and slightly weakened PV anomaly compared to the guess at the location of the cell.

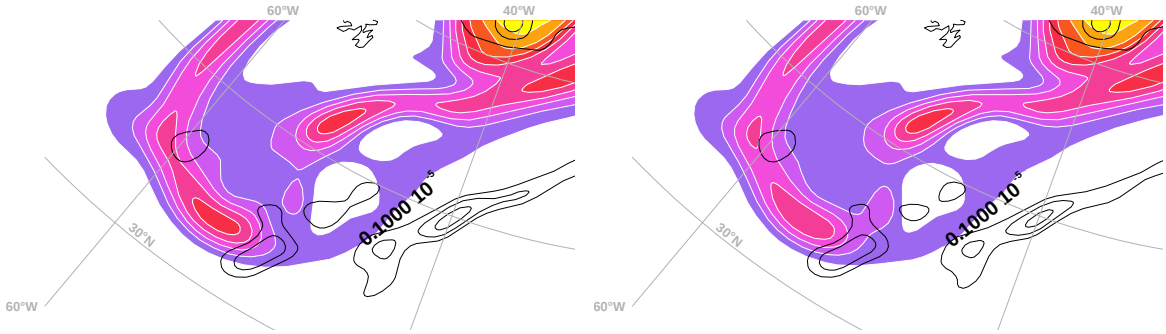

(a) The guess field (b) The analysis field

Figure 11: Correction of the PV initial state : PV fields at 300 hPa from ARPEGE on 26/05/2006 00UTC (contouring every 1 PVU starting 1 PVU) and relative vorticity at 850 hPa (contouring every $0.5s^{-1}$ starting $0.5s^{-1}$).

The assimilation of this PV observation leads to a limited but positive impact on the forecast. The figure 12 shows that after 24 hours, the cyclogenesis is 5 hPa less deep than the guess forecast but still more intense than the verifying analysis. PV increments interact through localized vertical velocities with the lower relative vorticity vortex (figure 13). Only a part of the analysis error is corrected. Reasons may include that just a few PV observations where presented to the data assimilation scheme and that the cyclogenesis was already strongly developing in the background field used for the assimilation.

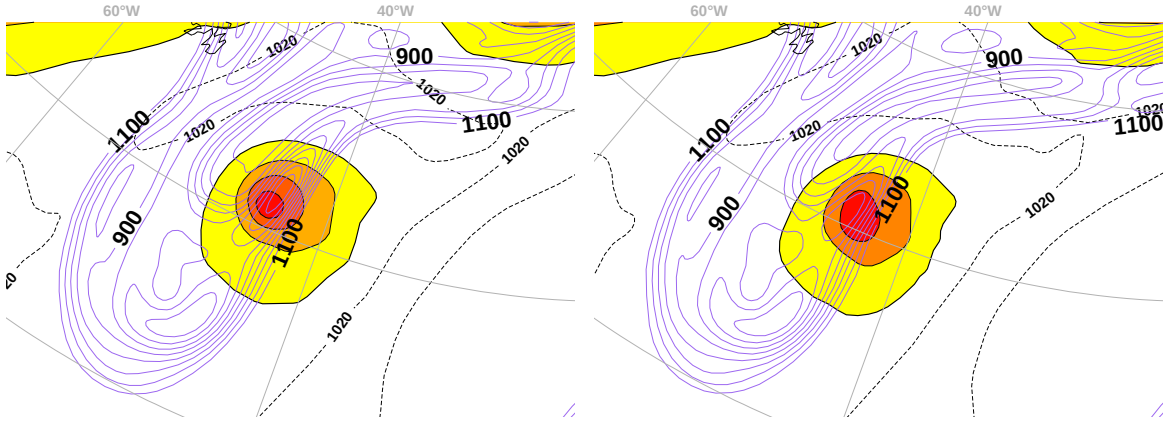

(a) 30 hours forecast from the guess (b) 24 hours forecast from the analysis of PV observations

Figure 12: Mean-sea level surface pressure (contouring every 5 hPa) and 1.5 PVU height (every 500 dam, in violet) valid for 27/05/2006, 00 UTC.

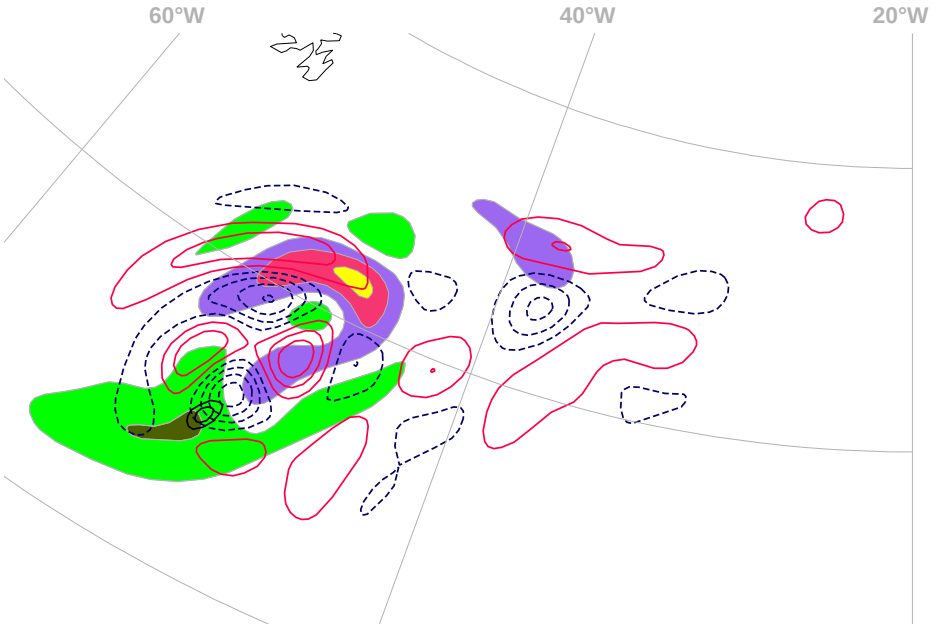

(a) Difference after 6 hours

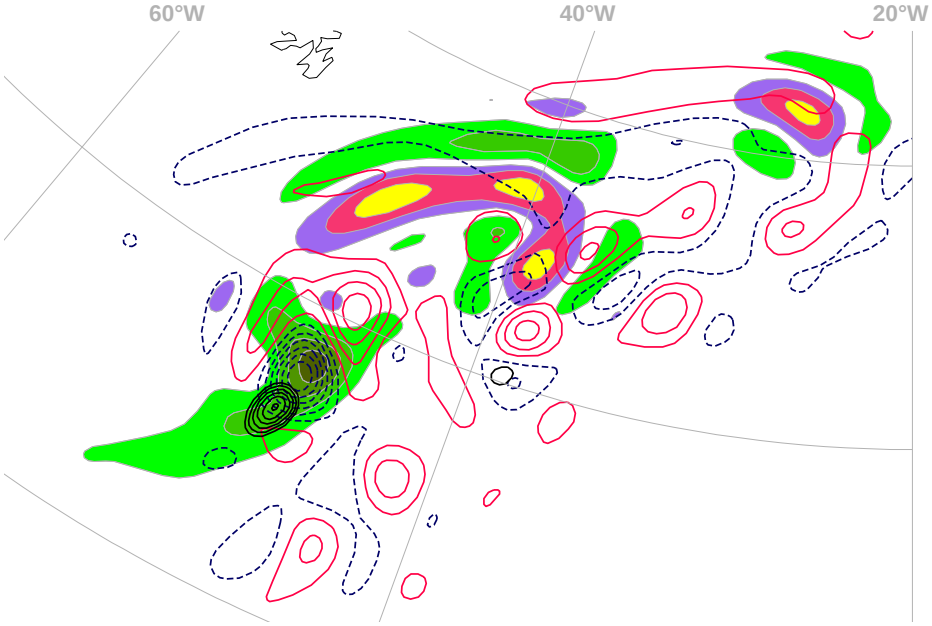

(b) Difference after 12 hours

Figure 13: Non-linear evolution of the increment (e.g. forecast from analysis minus forecast from background) at 300 hPa for 6 and 12 hours. The contouring of PV differences at 300 hPa is in grey (every 0.2 PVU, colour-shaded). Contouring of differences of vertical velocities at 700 hPa (red when positive, blue negative; contouring every 0.1 $Pams^{-1}$). Contouring of differences of relative vorticity at 850 hPa (bold contouring every 0.5 s^{-1}).

Conclusion

An algorithm has been developed that detects satellite imagery features likely to be associated with active upper tropospheric cyclones. It works in several steps. Sets of radiance temperature pixels that are significantly warmer than their environment are detected on individual images using a multi-thresholding algorithm. These sets, called "cells", are grouped into trajectories that span several consecutive images, based on overlapping and advection criteria. The spurious features are screened using several selection criteria. The lifetime criterion requires that trajectories of features last longer than a given threshold. The temperature criterion requires that each trajectory warms up at a minimum rate at its beginning, which is typical of dynamically active cyclones. The meteorological context criterion requires the use of a model output, and needs the trajectories to be close enough to an upper level jet stream and on its cyclonic side, for a significant time.

The detection and screening algorithm is tested on a sample of images over the North Atlantic and Europe. It is shown to detect all meteorologically significant cyclones, while detecting few spurious (i.e. not dynamically active) cyclones. The performance is similar when the algorithm is applied to simulated images from an operational global NWP model. A simple model/image object association technique is tested, which provides an easy visual comparison between forecast and observed upper tropospheric cyclones. The output can be interpreted in the light of the theory of PV dynamics and its interpretation in terms of water vapour satellite imagery.

This work demonstrates the feasibility of an automatic comparison between model and imagery, in terms of dynamically active upper tropospheric cyclones. Ongoing work deals with the relationship between the temperature of these dynamical cells and the potential vorticity fields. We show several cases where a qualitative agreement exists between radiance and averaged PV values under the cells. The relationship was shown to be degraded by analysis increments (when using 4D-Var trajectories for the cells), by apparent horizontal shifts between WV and PV fields and by the presence of localized maximum on PV vertical profiles (that do not impact the 1.5 PVU height but that appear in the temperature signal).

The assimilation of PV observations has been tested on a case of an ARPEGE bad forecast. The cyclogenesis has weakened compared to the guess run but is still to deep compared to the verifying analysis. The PV increments interact through localized vertical velocities with the lower relative vorticity vortex. The result is encouraging because just a few PV observations where presented to the 4D-Var assimilation scheme.

Future work will address the automatic specification of accurate PV observations and of their error statistics. One issue that should be covered is the detection of a tropopause foliation (when there are apparent shifts between WV and PV fields) in order to improve PV-WV relationship and the amplitude correction term. The study of the behaviour of PV observations and of their impact on cyclogenesis forecast will then be addressed more generally.

References

Andersson, E., Pailleux, J., Thepaut, J.N.,Eyre, J.R..,Mcnally, A.P.,Kelly, G.A.,Courtier, P, 1994: Use of cloud-cleared radiances in three/four-dimensional variational data assimilation *Q. J. R. Meteorol. Soc.*, **120,** 627–653

Andersson, E.,Fisher, M, Munro, R and Mcnally, A, 2000: Diagnosis of background errors for radiances and other observable quantities in a variational data assimilation scheme, and the explanation scheme, and the explanation of a case of poor convergence *Q. J. R. Meteorol. Soc.*, **126,** 1455–1472

Bormann, N, Saarinen, S,Kelly, G,Thepaut, J.N., 2003: The Spatial Structure of Observation Errors in Atmospheric Motion Vectors from Geostationary Satellite Data *Mon. Weather Rev.*, **131,** 706–718

Bouttier, F., 1993: The dynamics of error covariances in a barotropic model. *Tellus*, **51A,** 167–194

Daley, R., 1995: Estimating the Wind Field from Chemical Constituent Observations: Experiments with a One-Dimensional Extended Kalman Filter *Mon. Weather Rev.*, **123,** 181–198

Demirtas, M. and Thorpe, A, 1999: Sensitivity of short-range weather forecasts to local potential vorticity modifications. *Mon. Weather Rev.*, **127,** 922–939

Derber, J. and Bouttier, F, 1999: A reformulation of the background error covariance in the ECMWF global data assimilation system *Tellus*, **52A,** 195–221

Georgiev, C., 1999: Quantitative relationship between METEOSAT Water Vapour data and positive vorticity anomalies: a case study over the Mediterranean. *Meteorol. Appl.*, **6,** 97–109

Georgiev, C. and Martín, F., 2001: Use of potential vorticity fields, METEOSAT water vapour imagery and pseudo water vapour images for evaluating numerical model behaviour. *Meteorol. Appl.*, **8,** 57–69

Guérin, R., Desroziers, G. and Arbogast, P., 2006: 4D-Var analysis of pseudo potential-vorticity observations. *Q. J. R. Meteorol. Soc.*, **132,** 1283–1298

Hoffman, R.N., Louis, J-F. and Grassotti, C., 1995: Distortion representation of forecast errors. *Mon. Weather Rev.*, **123,** 2758–2770

Hoskins, B., McIntyre, M. and Roberson, A., 1985: On the use and significance of isentropic potential vorticity maps. *Q. J. R. Meteorol. Soc.*, **111,** 877–946

Joiner, J. and Dee, D.P., 2000: An error analysis of radiance and suboptimal retrieval assimilation. *Q. J. R. Meteorol. Soc.*, **126,** 1495–1514

Fischer, C.,Joly, A. and Lalaurette, F.,1998: Error growth and Kalman filtering within an idealized baroclinic flow *Tellus*, **50A,** 596–615

Lawson, W.G. and Hansen, J.A., 2005: Alignment Error Models and Ensemble-Based Data Assimilation *Mon. Weather Rev.*, **133,** 1687–1709

Michel, Y. and Bouttier, F., 2006: Automated tracking of dry intrusions on satellite water vapour imagery and model output. *Q. J. R. Meteorol. Soc.*, **132,** 2257–2276

Morel, C. and Sénési, S., 2002: A climatology of mesoscale convective systems over Europe using satellite infrared imagery. Part I: Methodology. *Q. J. R. Meteorol. Soc.*, **128,** 1953–1971

Peak, J., and Tag, P., 1994: Segmentation of satellite imagery using hierarchical thresholding and

neural networks. *J. Appl. Meteorol.,* **33,** 605–616

Pu, Z.X. and Braun, S.A., 2001: Evaluation of Bogus Vortex Techniques with Four-Dimensional Variational Data Assimilation *Mon. Weather Rev.,* **129,** 2023–2039

Røsting, B, Kristjánsson, J.E. and Sunde, J., 2003: The sensitivity of numerical simulations to initial modifications of potential vorticity–a case-study. *Q. J. R. Meteorol. Soc.,* **129,** 2697–2718

Røsting, B, Kristjánsson, J.E., 2006: Improving simulations of severe winter storms by initial modification of potential vorticity in sensistive regions *Q. J. R. Meteorol. Soc.,* **132,** –, In Press.

Santurette, P. and Georgiev, C., 2005: Weather analysis and forecasting: applying satellite water vapor imagery and potential vorticity analysis. *Academic Press,* 0-12-619262-6, 200pp.

Snyder, C.,Hamill, T.M. and Trier, S., 2003: Linear evolution of forecast error covariances in a quasigeostrophic model. *Mon. Weather Rev.,* **131,** 189–205

Swarbrick, S., 2001: Applying the relationship between potential vorticity fields and water vapour imagery to adjust initial conditions in numerical weather prediction. *Meteorol. Appl.,* **8,** 221–228

Velden, C., Hayden, C., Nieman, S., Menzel, P., Wanzong, S. and Goerss, J., 1997 Upper-tropospheric winds derived from geostationary satellite water vapor observations. *Bull. Am. Meteorol. Soc.,* **78(2),** 173–195

Weldon, R. and Holmes, S., 1991: Water vapour imagery: interpretation and applications to weather analysis and forecasting. *NOAA Technical Report, NESDIS 57.* NOAA, US Dept. of Commerce, Washington D.C.